Measurement of the x-ray mass attenuation coefficients of gold in the 38–50-keV energy range

M. T. Islam, N. A. Rae, J. L. Glover, Z. Barnea, M. D. de Jonge, C. Q. Tran, J. Wang, and C. T. Chantler*
School of Physics, The University of Melbourne, Parkville, Victoria 3010, Australia
(Received 18 August 2009; published 16 February 2010)

We used synchrotron x rays to measure the x-ray mass attenuation coefficients of gold at nine energies from 38 to 50 keV with accuracies of 0.1%. Our results are much more accurate than previous measurements in this energy range. A comparison of our measurements with calculated mass attenuation coefficients shows that our measurements fall almost exactly midway between the XCOM and FFAST calculated theoretical values, which differ from one another in this energy region by about 4%, even though the range includes no absorption edge. The consistency and accuracy of these measurements open the way to investigations of the x-ray attenuation in the region of the L absorption edge of gold.

DOI: 10.1103/PhysRevA.81.022903 PACS number(s): 32.80.Aa, 61.05.cj, 32.80.Fb, 78.20.Ci

I. INTRODUCTION

X-ray mass attenuation coefficients provide a wide variety of information about the fundamental properties of atomic, molecular, and solid-state materials [1,2]. Relative and absolute measurements of x-ray mass attenuation coefficients are used to provide information on the density of electronic states [3] and to test predictions of the photoabsorption [4–6] and elastic scattering [7,8] using bound-state electron wave functions. Absolute mass attenuation measurements provide additional, crucial, and demanding tests of theoretical predictions though relative measurements are adequate for some applications [9].

Discrepancies between various theoretically calculated x-ray mass attenuation coefficients of high-Z elements are larger than for low-Z elements. These discrepancies are of great concern. Comparing the two theoretical tabulations FFAST [10,11] and XCOM [12,13], which are recommended by the National Institute for Standards and Technology (NIST), discrepancies for elements with atomic numbers between 60 and 82 are 15–50% near the absorption edges and 2–5% throughout the high energy range.

There have been few previously published measurements of the mass attenuation coefficient of gold especially in the high energy range. Previous measurements were made using Bremsstrahlung radiation [14,15], but such studies have not had the accuracy or statistics to distinguish between different theoretical calculations.

Our motivation for measuring the x-ray mass attenuation coefficients of gold was to test our suite of measurement techniques, the X-ray Extended Range Technique (XERT) [16–18], for a high-Z element in an energy range clearly removed from the region of the K and L edges. At high energies x-ray absorption is almost purely an atomic effect. The different theoretical approaches should therefore agree in this region, to better than 1%, but do not. Measurements in this region are therefore useful in determining the pattern of discrepancies for different calculations in the purely atomic region. These measurements and their relationship to the theoretically predicted values will allow us to extend attenuation measurements to the region of the L absorption edge of gold in order to investigate any discrepancies with theoretical predictions in the vicinity of the L edge as opposed to discrepancies investigated near the K edges of different elemental systems [19–23]. The x-ray mass attenuation coefficients of gold were determined in the energy range between 38 and 50 keV with an uncertainty of 0.1%. This is one of the highest accuracies in the literature, especially for a high-Z element at high energies. The measured attenuation coefficients are compared with FFAST [10,11] and XCOM [12,13] tabulated values and with previous experimental measurements.

The measurements lie about half way between the XCOM and FFAST predictions. Unlike previous comparisons made with the XERT technique, the discrepancy is not an offset far above the K edge but is energy dependent. In this higher energy region we found a new and different pattern of discrepancies between high accuracy measurements and the FFAST and XCOM calculations.

II. EXPERIMENTAL TECHNIQUE

The experimental configuration is shown in Fig. 1. An x-ray beam was produced using a bending magnet at the 1-BM XOR beamline of the Advanced Photon Source (APS) synchrotron at the Argonne National Laboratory. The x-ray beam was monochromated by reflection from the (400) planes of a pair of silicon crystals located in the first optical enclosure. To define the beam cross section (of approximately 2×2 mm^2) the monochromated x rays passed through a pair of orthogonal adjustable slits. Ion chambers were located upstream and downstream from the attenuating foils for the beam intensity to be monitored and measured.

A six-circle Huber diffractometer was located downstream from the apparatus used for the attenuation measurement. A thin capillary filled with the silicon standard reference material SRM 640b was mounted on the central axis of the diffractometer. A sodium iodide scintillation counter located on the scanning arm of the diffractometer was used to record the angular location of a number of reflections from the powder sample. The monochromator was set to produce photons of energy well above 50 keV and then gradually stepped down to lower energies during the attenuation measurements to avoid the effects of backlash.

*chantler@physics.unimelb.edu.au

 ©2010 The American Physical Society

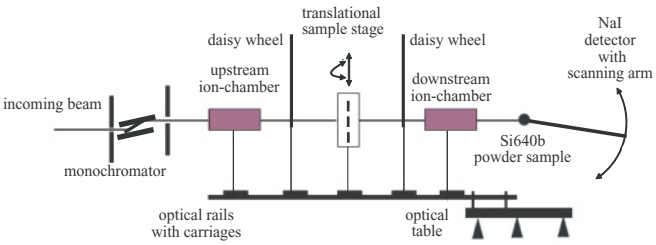

FIG. 1. (Color online) Schematic diagram of the experimental layout. This layout represents the experimental setup using the XERT at the APS from which data were collected for this analysis. Daisy wheels monitor harmonic contamination and scattering contributions. The Si640b powder sample calibrates energy.

III. DETAILED ANALYSIS

To analyze the raw data, which is a set of data for each sample and each energy containing upstream and downstream repeated measurements with different apertures and with ancillary measurements of energy, harmonics, and detector noise, we investigate the absolute determination of integrated column density in the next section. In following sections we discuss the processing of foil attenuation, energy calibration, harmonic contamination, and scattering data to obtain robust and accurate estimates of uncertainties for the final results.

A. Integrated column density

We used four gold foils with nominal thicknesses between 9.3 and 275 μm for the measurements. The purity of all the foils supplied by Goodfellow was approximately 99.99%. The masses of the foils were determined by weighing them four times using a microgram balance. The average of these measurements was taken to be the mass of each foil. The uncertainty in the mass was determined from the standard deviation of the repeated weighings. The mass m of the thickest (reference) foil was found to be $m = 3.390889 \pm 0.000003$ g. The area A of this foil was measured by using an optical comparator with resolution $5 \times 5\ \mu\text{m}^2$ and found to be $A = 662.199 \pm 0.176\ \text{mm}^2$. The average integrated column density $[\rho t]_{\text{av}}$ of the 275 μm reference foil was found to be $[\rho t]_{\text{av}} = 0.5121 g/\text{cm}^2 \pm 0.0002\ \text{g/cm}^2$.

To determine the integrated column density $[\rho t]_c$ at the center of the reference foil, we made an x-ray raster scan of the central $8 \times 8\ \text{mm}^2$ area of the foil from which we obtained the average $[\rho t]_{\text{av}}$ over the foil, illustrated by the central square in Fig. 2.

Micrometer measurements were also used to measure the average thickness profile of the foil with 0.5 μm precision. There were 25 micrometer measurements performed over the full $20 \times 20\ \text{mm}^2$ area of the foil. The average thickness t_{ff} of the reference foil (275 μm) can be scaled to the average column density from the mass per unit area. Then the regional average t_m of the reference foil for the central $8 \times 8\ \text{mm}^2$ region corresponding to the micrometer measurements is

$$t_m = \frac{\sum_i A_i t_i}{\sum_i A_i}, \tag{1}$$

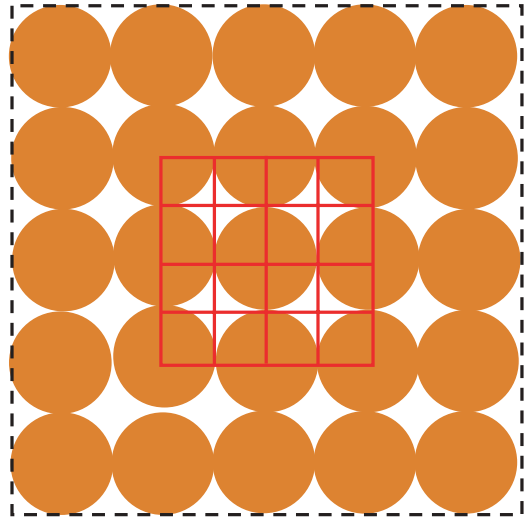

FIG. 2. (Color online) Micrometer measurements at the 25 points represented by the circles. The central area of the foil ($8 \times 8\ \text{mm}^2$) scanned by an x-ray beam is represented by the squares corresponding to nine micrometer measurements.

where A_i are the overlap coefficients of the ith micrometer map with x-ray beam. The corresponding uncertainty was determined by

$$\sigma_{t_m} = \sqrt{\sum \left(\frac{A_i}{\sum A_i}\right)^2 \sigma_{t_i}^2} = 3/8 \times 0.5 = 0.188\ \mu\text{m}. \tag{2}$$

The average of the n measurements was found to be $t_{\text{ff}} = 269.68 \pm 0.1\ \mu$m (0.037%), while the corresponding regional average t_m was found to be $269.25 \pm 0.188\ \mu$m ($\pm$0.074%). Making use of the scaling factor $t_{\text{ff}}/t_m = 1.002$, the attenuation over the full-foil $[\mu t]_{\text{ff}}$ is

$$[\mu t]_{\text{ff}} = \frac{t_{\text{ff}}}{t_m} \times [\mu t]_m, \tag{3}$$

where $[\mu t]_{\text{ff}}$ is the average attenuation over the full-foil and $[\mu t]_m$ is the average attenuation of the micrometer intersection x-ray map. The corresponding uncertainty was then

$$\sigma_{[\mu t]_{\text{ff}}} = \sqrt{\left(\frac{\sigma_{t_{\text{ff}}}}{t_{\text{ff}}}\right)^2 + \left(\frac{\sigma_{t_m}}{t_m}\right)^2 + \left(\frac{\sigma_{[\mu t]_m}}{[\mu t]_m}\right)^2}. \tag{4}$$

The $[\mu t]_{\text{ff}}$ were found to be $5.7866 \pm 0.10\%$ at 42 keV and $3.6683 \pm 0.11\%$ at 50 keV using Eq. (3). The corresponding uncertainty was determined by Eq. (4).

The attenuations of the reference foil at 42 and 50 keV are shown in Figs. 3(a) and 3(b), respectively. The attenuation $[\mu t]$ at each point of the raster scan was obtained following the subtraction of dark current and using

$$[\mu t] = -\ln\left[\frac{(I/I_0)_s}{(I/I_0)_b}\right], \tag{5}$$

where the subscript s refers to measurements made with a foil in the path of the beam and the subscript b refers to

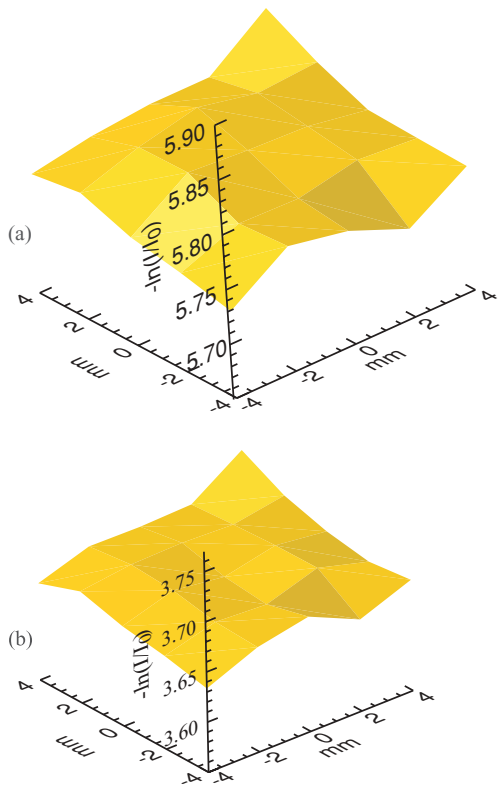

FIG. 3. (Color online) The two-dimensional x-ray maps of the attenuation $[\mu t]$ of the reference foil obtained from raster scans at (a) 42 and (b) 50 keV. The variations of foil attenuation on the maps were found to be within the range of $-0.64\% \rightarrow +0.74\%$ at 42 keV and $-0.72\% \rightarrow +1.02\%$ at 50 keV, respectively.

the measurements made without a foil. I and I_0 are the attenuated and unattenuated intensities, respectively, measured by the readings in the upstream and downstream detectors. The uncertainty of the measurements was determined from the uncertainties of the intensity measurements with and without the sample in the path of the beam.

The attenuation at the central point $[\mu t]_c$ of the reference foil and the average attenuation $[\mu t]_m$ were 5.7868 ± 0.0007 ($\pm 0.01\%$) and 5.7754 ± 0.0037 ($\pm 0.06\%$) at 42 keV and 3.6575 ± 0.0008 ($\pm 0.02\%$) and 3.6605 ± 0.0027 ($\pm 0.07\%$) at 50 keV. The integrated column density at the central point $[\rho t]_c$ was then determined making use of the attenuation at the central point $[\mu t]_c$, average attenuation over the full-foil $[\mu t]_{\mathrm{ff}}$, and the average integrated column density of the foil $[\rho t]_{\mathrm{ff}}$

$$[\rho t]_c = \frac{[\mu t]_c}{[\mu t]_{\mathrm{ff}}} \times [\rho t]_{\mathrm{ff}}, \tag{6}$$

where $[\rho t]_{\mathrm{ff}}$ is the average integrated column density ($= \mathrm{m}/A$). The corresponding uncertainty was

$$\sigma_{[\rho t]_c} = \sqrt{\left(\frac{\sigma_{[\mu t]_c}}{[\mu t]_c}\right)^2 + \left(\frac{\sigma_{[\mu t]_{\mathrm{ff}}}}{[\mu t]_{\mathrm{ff}}}\right)^2 + \left(\frac{\sigma_{[\rho t]_{\mathrm{ff}}}}{[\rho t]_{\mathrm{ff}}}\right)^2}. \tag{7}$$

The integrated column density $[\rho t]_c$ and the corresponding uncertainty were found to be $0.51214\ \mathrm{g/cm^2} \pm 0.11\%$ at 42 keV and $0.51066\ \mathrm{g/cm^2} \pm 0.12\%$ at 50 keV. The weighted mean of $[\rho t]_c$ obtained at the two energies was $0.5115\ \mathrm{g/cm^2} \pm 0.1\%$. The integrated column densities of other foils were determined by comparison with the reference foil, by using the attenuations of the foils at the energy where repeated measurements were performed following

$$[\rho t]_c = \frac{[\mu t]}{[\mu t]_R} \times [\rho t]_R, \tag{8}$$

where the subscript R refers to the reference foil and $[\mu t]$ is the measured attenuation of the other foil at 42 keV where multiple measurements were made. Table I shows the integrated column densities of the four gold foils.

TABLE I. The determined integrated column densities of the four gold foils. The weighted mean value of the column density of the reference foil determined at the two energies was $0.5115\ \mathrm{g/cm^2} \pm 0.1\%$. This value was used for determining the column densities of the other foils by a measurement relative to the reference foil at 42 keV.

$t_{\mathrm{nom}}(\mu\mathrm{m})$	$[\rho t](\mathrm{g/cm^2})$
275.0	$0.5115 \pm 0.10\%$
116.5	$0.2240 \pm 0.11\%$
100.6	$0.1972 \pm 0.12\%$
9.3	$0.0177 \pm 0.17\%$

B. Foil attenuation

To determine the attenuation of the gold foils, we used intensities recorded by the upstream u and downstream d ion chambers with a sample s placed in the x-ray beam, without a sample in the x-ray beam, and with the x-ray beam shutter closed to measure the dark current D. The attenuation $[\frac{\mu}{\rho}][\rho t]$ of each of the foils was determined from the negative of the logarithm of the transmission probability P given by

$$\left[\frac{\mu}{\rho}\right][\rho t] = -\ln P = -\ln\left[\overline{\left(\frac{I_d - D_d}{I_u - D_u}\right)_s} \Big/ \overline{\left(\frac{I_d - D_d}{I_u - D_u}\right)_b}\right], \tag{9}$$

where the subscript s refers to the intensity measured with a sample in the path of the beam and the subscript b refers to the intensity measured without a sample in the path of the beam. All intensity measurements of the downstream ion chamber were relative to the incident intensity recorded by the upstream ion chamber. The measured values of the foil attenuation as a function of energy are shown in Fig. 4.

The uncertainty in the attenuation was determined from the uncertainty contributions of the intensities measured with and without sample. The final uncertainty in the foil attenuation $[\frac{\mu}{\rho}][\rho t]$ was thus

$$\sigma^2_{[\frac{\mu}{\rho}][\rho t]} = \left[\sigma_{(\overline{[(I_d - D_d)/(I_u - D_u)]_s})}/(\overline{[(I_d - D_d)/(I_u - D_u)]_s})\right]^2 + \left[\sigma_{(\overline{[(I_d - D_d)/(I_u - D_u)]_b})}/(\overline{[(I_d - D_d)/(I_u - D_u)]_b})\right]^2, \tag{10}$$

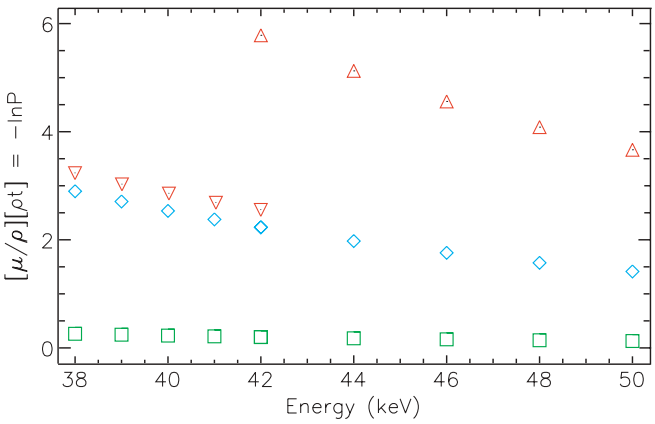

FIG. 4. (Color online) The foil attenuation was determined in accordance with Eq. (9). The symbol □ represents the attenuation by the foil with nominal thickness 9.3 μm, ◇ the nominal thickness of 100.6 μm, △ the nominal thickness of 275 μm, and ▽ the nominal thickness of 116.5 μm. Measurements for all four foils were made at 42 keV.

where s and b denote the measurements with and without a sample. $(\overline{I_d - D_d/I_u - D_u})$ represents the average of the intensities determined in each point measurement. The uncertainties of the measurements are shown in Fig. 5, with one being reported for the largest aperture and one for the smaller aperture. Note that the uncertainties (variance) of the larger aperture are greater.

C. Energy calibration

Powder diffraction patterns from the NIST standard reference powder Si 640b [$a_0 = 5.43094(11)$ Å] [24] were used to determine the energy at each monochromator setting at which calibration measurements were carried out [25,26]. The NIST standard powder sample was mounted on the six-circle Huber

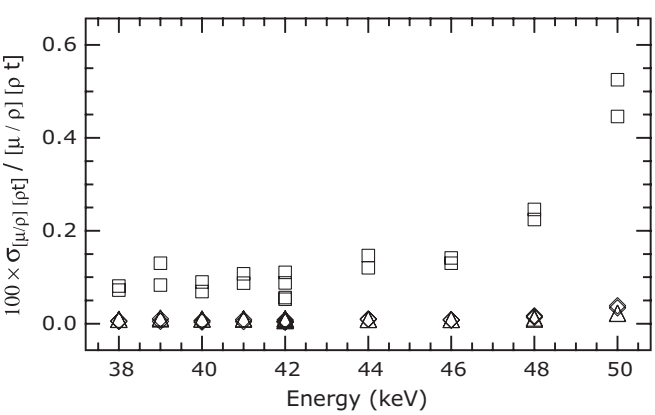

FIG. 5. The absolute values of the corresponding percentage uncertainties (standard errors) in individual foil attenuation measurements with symbols as in Fig. 4. The uncertainty varied from 0.01 to 0.5% for the thinnest 9.3 μm foil. Two measurements are plotted with the same symbol for two different aperture sizes used to collimate the beam and observe a signature for forward and backward scattering contributions. A higher uncertainty was found in attenuations determined with the largest size aperture. For foils other than the thinnest foil, the standard errors were 0.01 to 0.03%.

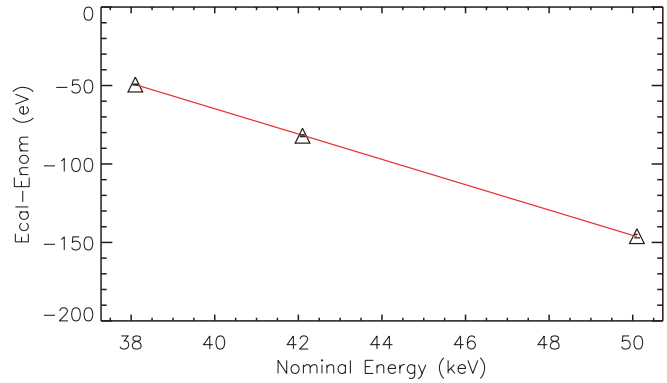

FIG. 6. (Color online) Difference between the energies E_{cal} derived from the powder patterns of the silicon standard and the nominal energies E_{nom} derived from the encoder reading between 38 and 50 keV. The known lattice parameter of the silicon standard was used to determine the energies of the beam. A linear interpolation was then applied to obtain all the energies at which the x-ray mass attenuation coefficients of gold were measured.

diffractometer. At each calibration energy the data comprise a number of individual peak scans made with an NaI scintillation detector mounted on a scanning arm centered on the powder diffraction sample. The powder diffraction peaks were fitted with a Lorentzian convolved with a slit peak profile with parameters of area, centroid, peak channel, and bandwidth. The energy was then determined by using the Bragg equation that related the monochromator angle directly to the energy

$$E = \frac{hc\sqrt{h^2 + k^2 + l^2}}{2a_0 \sin\theta}, \tag{11}$$

where (hkl) are the Miller indices of the reflecting planes, a_0 is the lattice parameter of the silicon standard, h is Planck's constant, c is the speed of light, and θ is the diffraction angle.

Three energies at about 50, 42, and 38 keV were calibrated by using the powder patterns. These energies were then used to calibrate the X-ray energies across the entire measurement range. The uncertainties of the three calibrated energies varied from 0.8 to 2 eV. The residuals were determined by using a covariance matrix. Figures 6 and 7 show the energy calibration and the uncertainties of the interpolated energies.

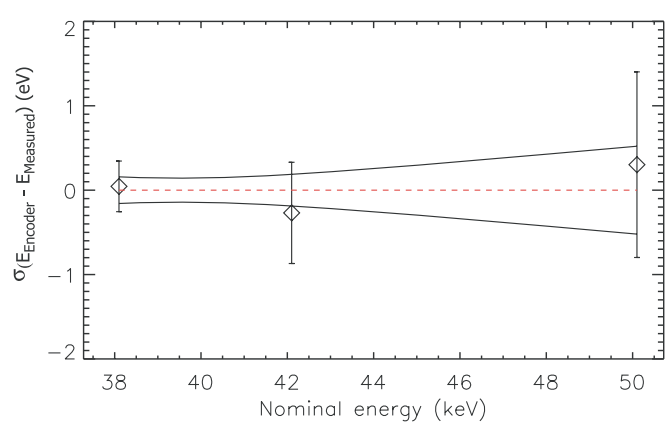

FIG. 7. (Color online) The envelope represents the uncertainties of the interpolated energies. The residuals were determined using a covariance matrix.

D. Effects due to harmonic contamination

The fundamental beam energy comes from the (400) Bragg peak of the silicon monochromator, while higher energy contributions to the beam may be present that correspond to higher order Bragg peaks, (600), (800), and (1200) for which the synchrotron produces photons of corresponding energy. Harmonic contamination of the beam is due to the contribution of higher energy Bragg peaks, which the monochromator accepts in addition to the fundamental energy of the monochromatized beam [27,28].

We used the different attenuation coefficient for the higher energy harmonic contamination to evaluate the effect of harmonic components in the x-ray beam on the determination of the mass attenuation coefficients. When harmonic components of energy E_n are present in the x-ray beam, the total transmission probability $\frac{I}{I_0}$ will be equal to the sum of the transmission probabilities for each of the energy components $\exp(-[\frac{\mu}{\rho}]_{E_n}[\rho t])$ weighted by the relative intensity of each component in the incident beam and the relative detection efficiency of each energy component. When there is only one harmonic component of energy E_n in a beam of fundamental energy E_1, the measured intensity ratio is [19]

$$\exp\left(-\left[\frac{\mu}{\rho}\right][\rho t]\right) = (1-f_n)\exp\left(-\left[\frac{\mu}{\rho}\right]_{E_1}[\rho t]\right) + f_n \exp\left(-\left[\frac{\mu}{\rho}\right]_{E_n}[\rho t]\right), \quad (12)$$

where f_n is the fraction of x-ray photons with energy E_n.

The fraction of the harmonic component was obtained by measuring the attenuation of multiple aluminum foils mounted on a daisy wheel [27]. We measured the attenuation of aluminum foils the thicknesses of which were chosen such that their attenuations $[\frac{\mu}{\rho}][\rho t]$ varied from 0.05 cm^2/g to 9.5 cm^2/g. Figure 8 shows the attenuation by the daisy wheel foils, measured using a beam of energy 39 keV. The dashed line drawn on the plot of Fig. 8 indicates the existence of a single harmonic component using the function defined in Eq. (12). There were no observable harmonic effects except at the two energies 38 and 39 keV as illustrated in Fig. 8. The harmonic effect on the measurements at these two energies is also at the one standard deviation level and the magnitude does not have a significant effect upon the results or uncertainties.

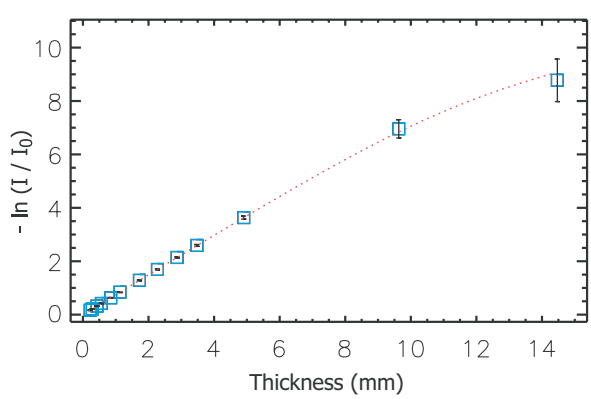

FIG. 8. (Color online) Results of daisy wheel measurements of the presence of harmonic radiation at 39 keV. This shows a clear deviation from linearity of the measured attenuation as a function of aluminum foil thickness measured at 39 keV. The harmonic fraction was $f_n = 0.004 \pm 0.003$.

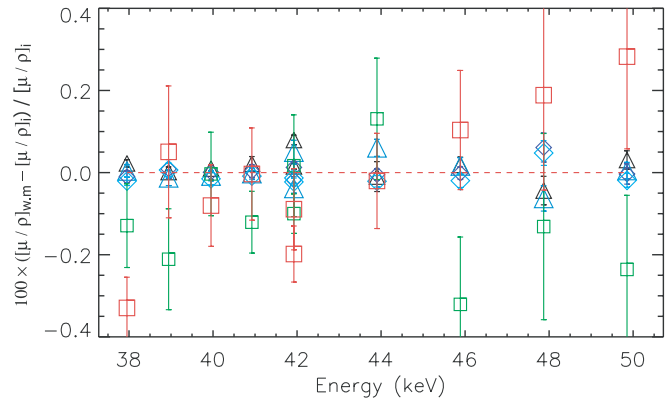

FIG. 9. (Color online) Percentage difference between the weighted mean and individual values of $[\frac{\mu}{\rho}]$ measured with different foil thicknesses and apertures. The symbols □ and ◇ represent the measurements for the 9.3 and 100.6 μm foils. The symbol △ represents the measurements for the 275 and 116.5 μm foils in the energy ranges 50–42 keV and 42–38 keV, respectively. The larger symbols of each pair correspond to measurements with the larger aperture. While there is a small trend for the (noisy) thinnest foil, each subset is indeed distributed around the mean and there is no residual signature of scattering.

E. Effect of scattered radiation

The effect of scattered radiation on the measured mass attenuation coefficients was investigated by observing the percentage variation between measurements obtained with different aperture sizes, sample thicknesses, and their weighted mean value. In fact, there is almost no signal for the thicker foils. While there might be a small effect for the thinnest foil, this seems dominated by noise (it changes sign Fig. 9). The effect of fluorescent radiation on the measured mass attenuation coefficients was not observed; the effect of fluorescent radiation being most significant in the vicinity of absorption edges [29]. Measured mass attenuation coefficients, away from the absorption edges, are not significantly affected by fluorescent radiation. Figure 9 shows that the effect of scattering on these results is insignificant.

IV. RESULTS AND DISCUSSION

A. The mass attenuation coefficients of gold

The mass attenuation coefficients of the foils were determined by dividing the foil attenuations $[\frac{\mu}{\rho}][\rho t]_c$ by the integrated column density $[\rho t]_c$ of the respective foils. For determining the mass attenuation coefficient of gold, four gold foils with different thicknesses were used in the energy range between 38 to 50 keV. To obtain the final attenuation coefficient $[\frac{\mu}{\rho}]$ at a given energy, we took the error weighted mean of $[\frac{\mu}{\rho}]$

TABLE II. Measured $[\frac{\mu}{\rho}]$ (second column) in the energy range between 37.95–49.86 keV with the values of $[\rho t]_c$ determined from a comparison with the reference foil. Numbers in parentheses are the standard deviations of the parameter in the least significant digits. The third column lists the percentage uncertainty contributed from the standard deviations of the measurements. The fourth column lists the final percentage errors $\sigma_{\rm tot}$ including the contribution from the uncertainty in the absolute value of $[\rho t]_c$, where $\%\sigma_{[\rho t]_c} = 0.1\%$. The fifth and sixth columns list the photoelectric mass absorption coefficient $[\frac{\mu}{\rho}]_{\rm pe}$ and the imaginary part of the atomic scattering factor f'', respectively.

$E_{\rm cal}$(keV)	$[\frac{\mu}{\rho}]$(cm^2/g)	$\sigma_{[\frac{\mu}{\rho}]_{\rm s.e.}}$	$\sigma_{[\frac{\mu}{\rho}]_{\rm tot}}$	$[\frac{\mu}{\rho}]_{\rm pe}$(cm^2/g)	$f''(e/\text{atom})$
37.95137(29)	14.6962(32)	0.022%	0.102%	13.6625(158)	2.4275(28)
38.94325(30)	13.7352(17)	0.012%	0.101%	12.7327(165)	2.3214(30)
39.95217(31)	12.8518(13)	0.010%	0.101%	11.8865(140)	2.2223(26)
40.92519(32)	12.0540(18)	0.015%	0.101%	11.1168(145)	2.1299(28)
41.92506(35)	11.3171(30)	0.027%	0.102%	10.4104(133)	2.0430(27)
43.90285(51)	10.0214(15)	0.015%	0.101%	9.1678(126)	1.8843(26)
45.88667(62)	8.9164(16)	0.018%	0.102%	8.1138(104)	1.7430(23)
47.87059(94)	7.9821(19)	0.024%	0.103%	7.2234(99)	1.6188(22)
49.8545(11)	7.1685(10)	0.014%	0.101%	6.4499(89)	1.5054(21)

obtained from the different foil thicknesses at that energy

$$\left[\frac{\mu}{\rho}\right] = \frac{\sum_{\rm all} [\frac{\mu}{\rho}]_i/\sigma^2_{[\frac{\mu}{\rho}]_i}}{\sum_{\rm all} 1/\sigma^2_{[\frac{\mu}{\rho}]_i}}, \tag{13}$$

where $[\frac{\mu}{\rho}]_i$ are the measured mass attenuation coefficients obtained from the different thicknesses and $\sigma_{[\frac{\mu}{\rho}]_i}$ are the corresponding errors of the measurements.

The final uncertainty in $[\frac{\mu}{\rho}]$ was estimated from the root mean square of the weighted mean uncertainty in $[\frac{\mu}{\rho}]$ and the error contribution from the integrated column density. This can be written as

$$\sigma_{[\frac{\mu}{\rho}]} = \sqrt{\frac{\sum_i \left(\frac{([\mu/\rho]_i - [\overline{\frac{\mu}{\rho}}])}{\sigma_{[\frac{\mu}{\rho}]_i}}\right)^2}{(N-1)\sum_i \frac{1}{\sigma^2_{[\frac{\mu}{\rho}]_i}}} + \left(\frac{\sigma_{[\rho t]_R}}{[\rho t]_R}\right)^2}, \tag{14}$$

where $[\overline{\frac{\mu}{\rho}}]$ is the weighted average of the $[\frac{\mu}{\rho}]_i$, $\sigma_{[\frac{\mu}{\rho}]_i}$ are the corresponding statistical errors in $[\frac{\mu}{\rho}]_i$, and N is the number of foils with different thicknesses measured at a given energy. The measured mass attenuation coefficients are listed in Table II.

B. Consistency of the determined $[\frac{\mu}{\rho}]$

We tested the consistency of the measured mass attenuation coefficients obtained with different foil thicknesses by investigating the percentage variation between the weighted mean and individual values. Figure 9 shows the percentage differences between the weighted mean values and the individual measurements with different foil thicknesses. The variation was found to be highest as expected for the thinnest foil, in the range between −0.3% and +0.4%.

C. The quantities of $[\frac{\mu}{\rho}]_{\rm pe}$ and f''

Experimentally, the photoelectric mass absorption coefficient $[\frac{\mu}{\rho}]_{\rm pe}$ is determined by subtracting the theoretically tabulated scattering cross sections $(\mu_R + \mu_C)$ from the measured attenuation coefficients $[\frac{\mu}{\rho}]$ [29]. In this analysis the $[\frac{\mu}{\rho}]_{\rm pe}$ was determined from the mass attenuation coefficients by subtracting the average of the Rayleigh plus Compton contributions $[\frac{\mu}{\rho}]_{R+C}$ as tabulated in FFAST [10] and XCOM [12]. The uncertainty in $[\mu/\rho]_{\rm pe}$ was determined from the error contributions in $[\frac{\mu}{\rho}]_{R+C}$, $[\frac{\mu}{\rho}]$, and $[\rho t]_R$. The uncertainty in the subtracted Rayleigh plus Compton contributions $[\frac{\mu}{\rho}]_{R+C}$ was estimated to be half of the difference between these tabulated values. The imaginary component f'' of the atomic form factor is directly related to the photoelectric mass absorption coefficient $[\frac{\mu}{\rho}]_{\rm pe}$ as

$$f'' = \frac{EuA[\frac{\mu}{\rho}]_{\rm pe}}{2hcr_e}, \tag{15}$$

where E is the photon energy in eV, u is the atomic mass unit, A the relative atomic mass of gold, h is Planck's constant, c is the speed of light, and r_e is the classical electron radius. The uncertainty in f'' is evaluated from

$$\sigma_{f''} = \frac{EuA}{2hcr_e}\left(\sigma^2_{[\frac{\mu}{\rho}]_{\rm pe}} + \Delta^2_{RC}\right)^{\frac{1}{2}}, \tag{16}$$

which includes an uncertainty contribution of half of the difference between the tabulated values of the Rayleigh and Compton contributions as tabulated in FFAST [10,11] and XCOM [12,13]. Table II presents the measured energies and the attenuation coefficients with their relative and absolute accuracies as discussed previously and then in the fifth and sixth columns lists the photoelectric mass absorption coefficient $[\frac{\mu}{\rho}]_{\rm pe}$ and the imaginary part of the atomic scattering factor f'' and their corresponding uncertainties.

D. Comparison of theory and experiment

NIST recommends two theoretical tabulations for the photoelectric absorption and Compton and Rayleigh scattering of x rays, which are used to calculate the mass attenuation coefficient. The recommended tabulations are FFAST [10,11] and XCOM [12,13]. We compared the measured x-ray mass attenuation coefficients of gold with both FFAST and XCOM tabulated values in Figs. 10 and 11. The solid line represents the FFAST values and the dashed line XCOM values. The results of this work are in somewhat better agreement with the FFAST tabulated values.

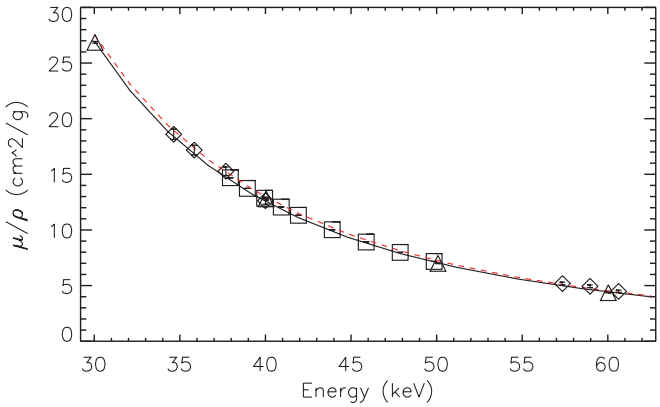

FIG. 10. (Color online) Comparison between the values of this work, two other experimental measurements, and the two theories FFAST and XCOM. The symbol □ represents the experimental values of this work (with error bars smaller than symbol sizes), the solid line represents FFAST values, and the dashed line represents the XCOM values. The symbol △ represents the values measured by J. H. McCrary *et al.* [30] and the symbol ◇ represents the experimental values presented by S. Laubert [31].

Experimental measurements of x-ray mass attenuation coefficients of gold are very limited in this energy range. It is notable that there are few values measured over an extended energy range [30–33]. We compare the values of this work with two data sets [30,31] over the energy range between 30–62 keV. In Fig. 10, plotted in the conventional manner, all experimental and theoretical values in the region appear to be in excellent agreement and it appears that both theoretical and experimental methods are sound, even including older experimental work and despite the relatively large error bars cited in their respective publications.

Alas, this is not so, as the crucial Fig. 11 reveals. Here all results are plotted on a finer scale relative to the theoretical tabulation of FFAST so that differentials, discrepancies, and problems can be identified. The measurements of the current article are characterized by the small error bars, much smaller than the others. Theoretical tabulations estimate uncertainties in this region as approximately 1%. The figure suggests that this might be an underestimate, but is likely correct within a factor of 2 or so. Agreement is slightly better with FFAST, overall, although perhaps the key point is that the experimental values lie almost midway between the two theoretical tabulations. Incidentally, the plot is relative to FFAST, but can be made relative to *any smooth function* to display the consistencies and inconsistencies. Hence the crucial detail about a reference theory (or experiment) for this comparative purpose is that it must be a smooth function. The figure shows that, in this region, FFAST, the experimental data, and XCOM are all smooth functions.

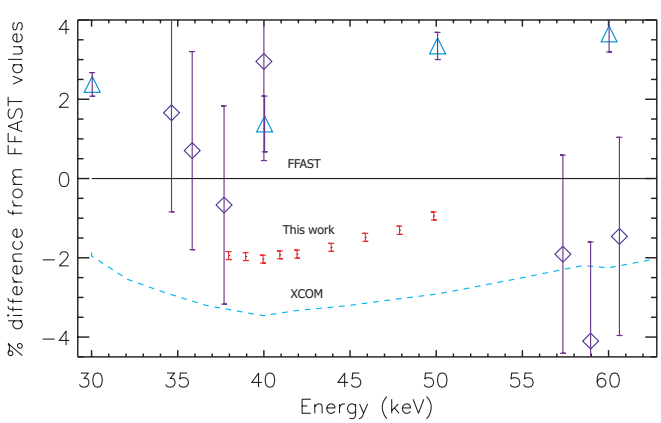

FIG. 11. (Color online) The percentage differences between this work, two other experimental measurements, and the two theories FFAST and XCOM are shown. The measured values, represented by the error bars without symbols, fall approximately midway between the FFAST and XCOM tabulated values in the energy range between 38 and 50 keV. The other single measurements represented by the symbols △ and ◇ were measured by J. H. McCrary *et al.* [30] and S. Laubert [31], respectively.

Conversely the older experimental data of McCrary and Laubert are not smooth, although their point-to-point precision is typically within two standard deviations. This reveals something important—Laubert, in particular [31], appears to give an uncertainty estimate that is an underestimate of his *precision*; the absolute accuracy is likely to be at least a little worse than this. In a similar manner, the point-to-point consistency of McCrary *et al.* [30] implies a precision about a factor of 2 larger than the uncertainties represented, but in this case both theories and our measurements suggest a large systematic error in the region of 2 to 4%, or some four to eight times the estimated uncertainty.

We argue that this is a key justification for a careful treatment of systematic sources of uncertainty. Turning critically to our measurements, we find a pattern not previously seen in any earlier experimental results (for any element)—the FFAST values lie above the XCOM values and our experimental data lie between the two tabulations. In past investigations, we saw a crossover or a systematic appearing like a dispersion function. Here, however, we see a smooth differential possibly indicative of a small and smooth convergence issue for the inner-shell wave functions of the gold atom. It can be argued that the gold sample is a solid foil and that condensed matter theory is necessary to elucidate this. Condensed matter theory necessarily has larger uncertainty than atomic computations, so will be unlikely to yield a clear result in this regime; we already see two atomic computations straddling the experimental answer, suggesting that the discrepancy is quite likely dominated by differential convergence. Further, in this regime, so far above the L shell and so far below the K edge, it is expected that the computation should be well represented by atomic properties. Recent speculation considered a differential (constant or slowly varying) offset due to solid-state effects or a peculiar oscillatory function (which of course will then impair apparent point-to-point smoothness). We only note that, obviously, such effects are not revealed by the data.

In regions of energy far from absorption edges as in this article, many-body effects and QED contributions are insignificant in the calculation of the total scattering cross section and cannot account for the discrepancies between theory and experiment as seen in Figure 11.

The calculations of XCOM are Hartree-Slater (nonrelativistic with relativistic corrections included in perturbation) while those of FFAST are Dirac-Hartree-Fock relativistic using Kohn-Sham potentials for effective screening. It is not expected that

the relativistic versus nonrelativistic nature of the calculations can explain the discrepancies seen. The level of convergence of the wave functions is a plausible source of difference between the calculations [10], however, convergence effects are highest near absorption edges, unlike the energy range investigated here.

Both calculations use an independent particle approximation (IPA). This approximation neglects some effects of the correlation between wave functions. Election correlation effects can be up to 20–30% to the incoherent scattering function [10]. Calculations that avoid the IPA such as multiconfigurational Hartree-Fock can be made at a small set of selected energies for gold and compared with the measurements presented here. However, given that the discrepancies are of opposite sign for different implementations, the signature is not due to this approximation *per se*.

Another source of an oscillatory discrepancy in theoretical calculation was identified as due to the accumulation of minor errors in inner shells and the electronic wave function distributions. This error is small for the K and L_I edges, but can be quite significant for the L_I, L_{II}, M_{IV}, and M_V, which occur at 13.73, 19.18, 22.9, and 22.05 keV, respectively, for gold. Given the energy range investigated here, it is not expected that this possible cause will be relevant; however, it will be worthwhile to investigate further.

In recent work, one of the most advanced theoretical solid-state groups investigated the effects of (i) core-hole lifetimes, (ii) threshold energy cutoff, (iii) the so-called edge singularity effect, (iv) multipole effects, and (v) embedded atomic background and solid-state local interactions [34]. However, although these effects can explain minor offsets at high energies they do not appear to explain the discrepancy observed here.

Figure 11 shows significant differences between our work and previous experimental results. The trend of the measurements made by Ref. [30] differs from our results by 2.5–3%, which is much greater than the error bars of either sets of measurements. The results of Ref. [31] are somewhat consistent within the large spread and error bars of those measurements. The large differences seen between experiments and theoretical calculations indicate the importance of high-accuracy measurements in this energy region.

V. CONCLUSION

We used the XERT to determine the x-ray mass attenuation coefficients of gold on an absolute scale at nine energies between 37.95 and 49.86 keV. This is the first time XERT was applied at such high energies and for such a high-Z element as gold. The resulting values with accuracies of 0.1% show that these measured mass attenuation coefficients fall approximately midway between the values theoretically calculated by the XCOM and FFAST methods, with the agreement being slightly better with the FFAST values.

The accuracy of our results will enable us to apply the same measurement and analysis techniques to the highly interesting region of the L absorption edge of gold and other high-Z elements. This investigation calls for further experimental investigations at higher energies to both consider the utility of the XERT in critical studies or where theoretical divergence is observed and to consider finer spacing; particularly focusing on regions where solid-state structure is known to significantly modify the absorption coefficient (namely in the XAFS regions, L edges, and K edges).

ACKNOWLEDGMENTS

This work was funded by the Australian Research Council (ARC). The authors wish to thank the staff of APS where the experiment was performed. We acknowledge the Australian Synchrotron Research Program (ASRP) for their support of this work.

[1] J. Rehr and R. Albers, Rev. Mod. Phys. **72**, 621 (2000).
[2] Y. Joly, Phys. Rev. B **63**, 125120 (2001).
[3] F. M. Hossain, D. P. Riley, and G. E. Murch, Phys. Rev. B **72**, 235101 (2005).
[4] L. Gerward, G. Thuesen, S. Jensen, and I. Alstrup, Acta Crystallogr. Sect. A **35**, 852 (1979).
[5] L. Gerward, Acta Crystallogr. Sect. A **45**, 1 (1989).
[6] A. Karabulut, A. Gurol, G. Budak, and M. Ertugrul, Nucl. Instrum. Methods Phys. Res. B **227**, 485 (2005).
[7] A. N. Hopersky, I. D. Petrov, A. M. Nadolinsky, V. A. Yavna, and R. V. Koneev, J. Phys. B **37**, 3313 (2004).
[8] A. Khoperskii, A. Nadolinskii, V. Yavna, and R. Koneev, Opt. Spectrosc. **98**, 161 (2005).
[9] A. Kodre, J. Padežnik Gomilšek, A. Mihelič, and I. Arčon, Radiat. Phys. Chem. **75**, 188 (2006).
[10] C. T. Chantler, J. Phys. Chem. Ref. Data **29**, 597 (2000).
[11] C. T. Chantler, J. Phys. Chem. Ref. Data **24**, 71 (1995).
[12] M. J. Berger and J. H. Hubbell, XCOM: Photon Cross Sections on a Personal Computer, NBSIR 87-3597 National Bureau of Standards, Gaithersburg, MD, 1987.
[13] E. B. Saloman, J. H. Hubbell, and J. H. Scofield, At. Data Nucl. Data Tables **38**, 1 (1988).
[14] S. Hosur, L. Naik, and N. Badiger, J. Phys. B **42**, 035002 (2009).
[15] S. Nayak and N. Badiger, J. Phys. B **39**, 2893 (2006).
[16] C. T. Chantler, C. Q. Tran, D. Paterson, and Z. Barnea, Phys. Lett. **A286**, 338 (2001).
[17] C. T. Chantler, C. Q. Tran, Z. Barnea, D. Paterson, D. Cookson, and D. X. Balaic, Phys. Rev. A **64**, 062506 (2001).
[18] M. D. de Jonge, C. Q. Tran, C. T. Chantler, and Z. Barnea, Opt. Eng. **45**, 046501 (2006).
[19] M. D. de Jonge, C. Q. Tran, C. T. Chantler, Z. Barnea, B. B. Dhal, D. J. Cookson, W. K. Lee, and A. Mashayekhi, Phys. Rev. A **71**, 032702 (2005).
[20] C. Q. Tran, C. T. Chantler, Z. Barnea, M. D. de Jonge, B. B. Dhal, C. T. Y. Chung, D. Paterson, and J. Wang, J. Phys. B **38**, 89 (2005).
[21] M. D. de Jonge *et al.*, Phys. Rev. A **75**, 032702 (2007).
[22] C. T. Chantler, C. Q. Tran, Z. Barnea, D. Paterson, D. J. Cookson, and D. X. Balaic, Phys. Rev. A **64**, 062506 (2001).

[23] J. L. Glover, C. T. Chantler, Z. Barnea, N. A. Rae, C. Q. Tran, D. C. Creagh, D. Paterson, and B. B. Dhal, Phys. Rev. A **78**, 052902 (2008).
[24] E. Parrish, A. J. C. Wilson, and J. I. Langford, *International Table for X-ray Crystallography* (Kluwer, Dordrecht, 1999) Vol. C, Sec. 5.2.10.
[25] C. T. Chantler, N. A. Rae, and C. Q. Tran, J. Appl. Crystallogr. **40**, 232 (2007).
[26] N. A. Rae, C. T. Chantler, C. Q. Tran, and Z. Barnea, Radiat. Phys. Chem. **75**, 2063 (2006).
[27] C. Q. Tran, Z. Barnea, M. D. de Jonge, B. B. Dhal, D. Paterson, D. J. Cookson, and C. T. Chantler, X-Ray Spectrom. **32**, 69 (2003).
[28] Z. Barnea and J. Mohyla, J. Appl. Crystallogr. **7**, 298 (1974).
[29] C. Q. Tran, M. D. de Jonge, Z. Barnea, and C. T. Chantler, J. Phys. B **37**, 3163 (2004).
[30] J. H. McCrary, E. H. Plassmann, J. M. Puckett, A. L. Conner, and G. W. Zimmermann, Phys. Rev. **153**, 307 (1967).
[31] S. Laubert, Ann. Phys. (Leipzig) **40**, 553 (1941).
[32] B. L. Henke, E. M. Gullikson, and J. C. Davis, At. Data Nucl. Data Tables **54**, 181 (1993).
[33] N. Kerr Del Grande, in *Proceedings of SPIE 691* "*X-ray Imaging II*" *(1986)*, pp. 2–10 (especially p8) (SPIE, Bellingham, WA, 1986).
[34] J. J. Kas, J. J. Rehr, J. L. Glover, and C. T. Chantler, Nucl. 737 Instrum. Methods A (2010, in press).